

# **Advanced Laboratory Course**

## **K223: Nuclear $\gamma\gamma$ Angular Correlations**

Amelia Carina de Lope Fend, Martin Ludwig

18.03.2025

# Contents

<b>1. Introduction</b>	<b>1</b>
<b>2. Theoretical Background</b>	<b>2</b>
2.1. Radioactive Decay of $^{60}_{27}\text{Co}$	2
2.2. Theoretical Prediction for the Angular Correlation Function	2
<b>3. Experimental Setup</b>	<b>4</b>
3.1. Detector Setup	4
3.2. Electronic Setup	5
3.2.1. Slow Branch	5
3.2.2. Fast Branch	5
3.2.3. Combining Both Branches	6
<b>4. Preparation and Calibration of the Setup</b>	<b>7</b>
4.1. Gain Adjustment of the Main Amplifiers	7
4.2. Calibration of the SCAs	8
4.3. Threshold Adjustment of the CFDs	10
4.4. Delay Adjustment	11
4.4.1. Fast Branch	12
4.4.2. Slow Branch	14
<b>5. Main Measurement</b>	<b>15</b>
5.1. Choice of Detector Distances	15
5.2. Choice of Measured Angles	16
5.3. Random coincidences	17
5.4. Stability Analysis	18
5.5. De-adjustment Correction	22
5.6. Angular Correlation	24
<b>6. Conclusion</b>	<b>26</b>
<b>A. Appendix</b>	<b>27</b>
A.1. Prompt Curve	27
A.2. Stability Analysis	28
<b>List of Figures</b>	<b>29</b>
<b>List of Tables</b>	<b>30</b>



# 1. Introduction

Radiation from radioactive nuclei is, under normal conditions, isotropic. However, in certain cases, such as in a cascaded decay, there is an angular correlation between consecutively emitted photons. In this experiment, we will study the radioactive decay of  $^{60}_{27}\text{Co}$ , which undergoes  $\beta^-$  decay into  $^{60}_{28}\text{Ni}^*$ . The excited nickel nucleus then emits two photons in quick succession, whose angular correlation will be determined.

This report is structured as follows: Chapter 2 briefly describes the decay scheme of  $^{60}_{27}\text{Co}$  and the expected distribution of the emitted photons. Chapter 3 introduces the experimental setup and the principles of the applied fast-slow coincidence circuit. Chapter 4 details the preparation and calibration steps leading to the main measurement, while Chapter 5 focuses on the setup and analysis of this main measurement. Finally, Chapter 6 summarizes our results.

## 2. Theoretical Background

### 2.1. Radioactive Decay of $^{60}_{27}\text{Co}$

To analyze the angular correlation of photons in cascaded decays, this experiment utilizes the radioactive decay of the isotope  $^{60}_{27}\text{Co}$ . This isotope decays via  $\beta^-$  emission, predominantly into the excited  $4^+$  state of  $^{60}_{28}\text{Ni}$ . This state then decays to the excited  $2^+$  state by emitting a 1173.2 keV photon, which subsequently decays to the ground state through the emission of a 1332.5 keV photon. This sequence is referred to as a 4(2)2(2)0 cascade, where the numbers in parentheses indicate the angular momentum of the emitted photon and the numbers outside denote the nuclear spin. This information is based on the decay scheme shown in Figure 2.1 taken from [1]. The successive decays of the excited  $^{60}_{28}\text{Ni}$  nucleus occur on a very short time scale of picoseconds and are therefore well suited for studying their angular correlation.

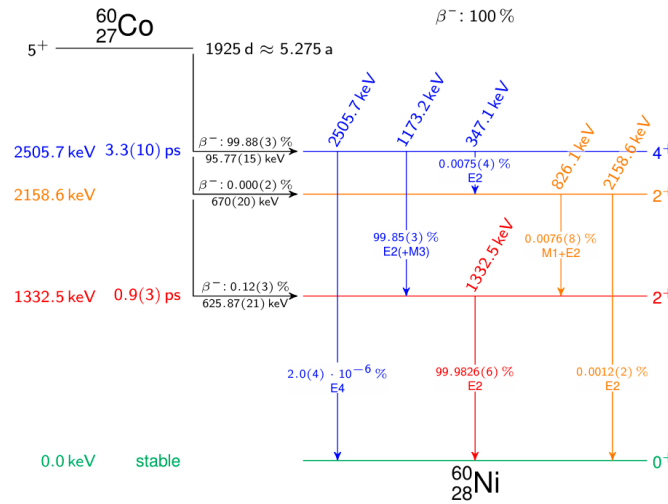


Figure 2.1.: Decay scheme of  $^{60}_{27}\text{Co}$ . Taken from [2].

### 2.2. Theoretical Prediction for the Angular Correlation Function

The information presented in this section is based on [3]. In thermal equilibrium, the total angular momenta of nuclei are randomly oriented in space, so we expect their total radiation to be distributed isotropically. A non-random orientation can be achieved

by strong magnetic fields or strong electric field gradients at very low temperatures. However, there is another possibility that is easier to realize in a laboratory. If a collection of nuclei decays by successive emission of radiation, one can use the first emission to select a group of nuclei with a non-isotropic distribution of total angular momentum. The angle of the second decay will then be correlated with that of the first decay.

For the  $4(2)2(2)0$  cascade of  $^{60}_{28}\text{Ni}$ , we expect the correlation function to be

$$W(\theta) \propto 1 + A_{22} \cdot P_2(\theta) + A_{44} \cdot P_4(\theta), \quad (2.1)$$

where  $P_n(\theta)$  are the Legendre polynomials of degree  $n$ . The theoretical prediction of the coefficients  $A_{22}$  and  $A_{44}$  is given on page 1033 of [3] as

$$A_{22} = 0.1020 \quad \text{and} \quad A_{44} = 0.0091. \quad (2.2)$$

## 3. Experimental Setup

### 3.1. Detector Setup

In this experiment, we aim to measure the angular correlation of the cascaded  $^{60}\text{Ni}$  decay. As mentioned in Section 2, this requires preselecting an ensemble of nuclei with a non-isotropic distribution of total angular momenta. We achieve this by fixing the angle between both detectors, which are positioned at equal distances from the  $^{60}\text{Co}$  source. This setup ensures that only nuclei emitting the first photon at a specific angle are detected. As a result, the quantization axis is defined, and we can expect the emission angle of the second photon to be correlated.

Both detectors consist of inorganic scintillators (NaI(Tl)) coupled with a photomultiplier. The photons in the cascaded decay are emitted on a timescale of picoseconds [1], which is much smaller than the setup's resolution time [4]. Therefore, we can assume that any photon pair detected in coincidence and matching the transition energies originates from the same decay (except for random coincidences, see Section 5.3).

To measure the correlation as a function of angle, the angle  $\theta$  between the detectors is adjustable. This motivates the setup shown in Figure 3.1, where the source and Detector 2 are fixed, while Detector 1 is movable.

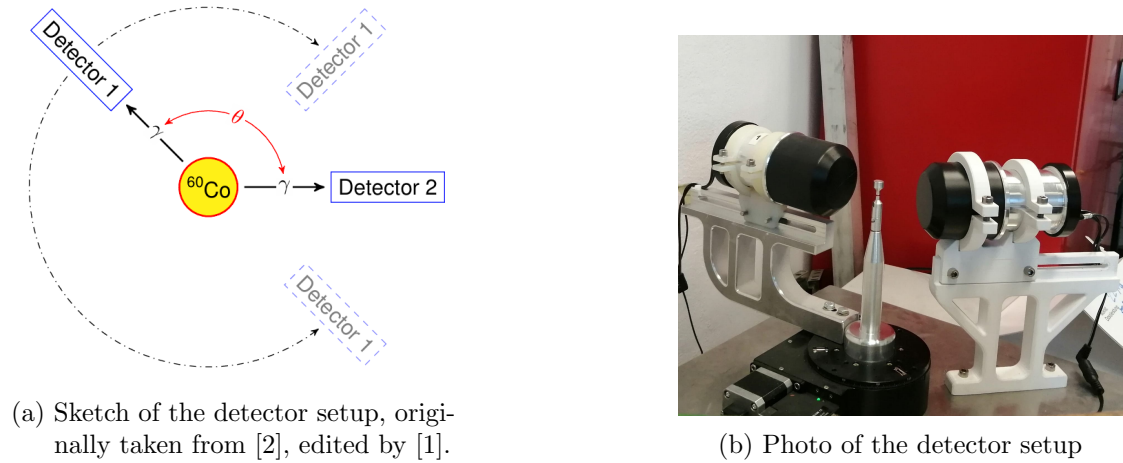


Figure 3.1.: Detector setup

## 3.2. Electronic Setup

To measure the coincidences and count rates, we need to expand the detector setup by a fast-slow coincidence. This is shown in Figure 3.2. The circuit consists of a fast branch and a slow branch component.

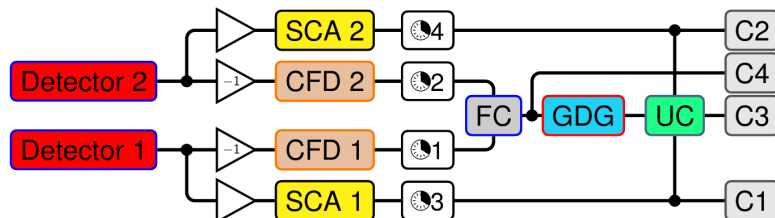


Figure 3.2.: Full setup of the fast-slow coincidence, taken from [2]

### 3.2.1. Slow Branch

The slow branch of the circuit is responsible for selecting photons whose energies correspond to the  $^{60}\text{Ni}$  transitions we want to observe. To implement this energy selection, the signal from each detector is first processed individually. This involves amplifying the signal before it is analyzed by a Single Channel Analyzer (SCA). The SCA allows for the selection of an energy window, defined by a lower and an upper threshold. Only photons with energies within this interval produce a square pulse, while any other photon yields no signal. To achieve energy selection, these windows must be adjusted to match the corresponding transition energies. Each individual SCA signal is then passed through a delay to compensate for additional delays caused by differences in cable lengths and other systematic effects.

Next, each signal is split: one part is sent to counters C1 and C2, respectively, which record the number of photons with matching energies detected by each detector. The other part is forwarded to a universal coincidence unit (UC), which combines information from both the fast and slow branches. Before discussing the role of the coincidence unit in detail, it is useful to first consider the fast branch.

### 3.2.2. Fast Branch

The fast branch evaluates the timing of the arriving photons. As mentioned above, the time difference between the emissions is much shorter than the resolution time of the detectors, so we detect photons from the same decaying nucleus as arriving at the same time. This branch ensures that only pairs of photons that fulfill this condition are considered when evaluating coincidences.

To implement this time selection, again each signal is first processed individually. After amplification, the signal is sent to a Constant Fraction Discriminator (CFD). The CFD triggers when the input signal reaches a certain fraction of its total amplitude. This preserves the timing information because the triggering moment does not depend



on the signal's amplitude, which may vary. The CFDs are also equipped with adjustable thresholds to help eliminate noise. Following the CFDs, delays are introduced to compensate for possible differences in the arrival times of each CFD signal (analogous to the slow branch).

Then, the individual signals from both detectors are sent to a fast coincidence unit (FC), which functions as a logical AND. The output of the fast coincidence is split: one part is registered by counter C4, which records the number of fast coincidences (for which the energy criterion is not necessarily fulfilled), and the other part is processed by a Gate and Delay Generator (GDG). The GDG is used to reshape and delay the pulse. Reshaping is necessary because, depending on the relative arrival times of the CFD pulses, the FC may output a relatively short signal that is unsuitable for the UC.

### **3.2.3. Combining Both Branches**

The task of the universal coincidence (UC) is to combine the signals from both branches and act as a logical AND. Only if the detected photons arrive simultaneously (triggering the FC) and have the correct energies (triggering the SCAs) the UC produces an output signal. This signal is recorded by counter C3. Both true coincidences and random coincidences are registered, with the latter needing to be estimated later and subtracted from the measurement, see Section 5.3.

## 4. Preparation and Calibration of the Setup

We will construct the fast-slow coincidence setup introduced in Chapter 3 step by step. This approach ensures that each component is properly calibrated and functions as expected. Additionally, measuring the spectra of individual components before assembling the full circuit allows us to analyze their properties, such as the sensitivity of the SCAs and the CFDs. Information regarding the functioning of the electronic components is taken from [4].

### 4.1. Gain Adjustment of the Main Amplifiers

The first step is to set the gain of the amplifiers so that the signal amplitude is as high as possible while remaining below the maximum allowable amplitude of the electronics, 10 V. We aim for an amplitude in the range of 8 to 9 V. To achieve this, we assemble a simple circuit, as shown in Figure 4.1. The signal from the detector is processed by the amplifier, and the amplifier's output is displayed on an oscilloscope as well as used as input for a Multi-Channel Analyzer (MCA).

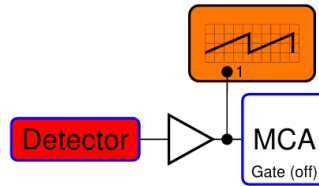


Figure 4.1.: Circuit used to adjust the gain of the amplifier. This is done for each detector. Taken from [2], edited by [1]

We use the MCA without gate, so that every signal is detected. On the lab computer's screen, a typical scintillator spectrum is observed, including the Compton edge and continuum and a backscatter peak at lower energies, as well as the two photo peaks at higher energies. By adjusting the gain, the position of the photo peaks is shifted. If the gain is set too high, the photo peaks eventually disappear from the spectrum because they correspond to energies beyond the available channels.

Figure 4.2 shows the oscillograms of the detector pulses after amplification. Since the amplifier's bipolar output is used, the signal exhibits a zero-crossing. Its amplitude reaches the intended 8 to 9 V for most pulses. A higher gain would have led to saturation, meaning the signal's peaks would have been clipped.



(a) Movable detector (D1)



(b) Fixed detector (D2)

Figure 4.2.: Oscillograms of the detector pulses after amplification. Each square of the grid corresponds to 500 ns in the horizontal direction and 5 V in the vertical direction.

## 4.2. Calibration of the SCAs

The next goal is to adjust the windows of the SCAs so that the selected pulses correspond to the photo peaks of the spectrum. For this purpose, we set up the circuit shown in Figure 4.3.

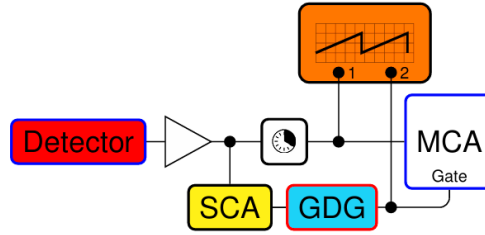


Figure 4.3.: Circuit used to set the windows of the SCAs. This is done for both detectors. Taken from [2].

In this configuration, the signal from the detector is amplified and then split. One part is forwarded to a delay and then to the MCA, while the other part is processed by the SCA, followed by the GDG, and is used as a gate signal for the MCA. Additionally, both parts are observed with the oscilloscope to determine their relative positions. By adjusting the delay, the signals are shifted so that they coincide, as shown in Figure 4.4.

With this adjustment, we can record the spectrum with the MCA, allowing us to directly observe the range over which the SCA windows extend. Now we have two options: We can either adjust the windows so that each SCA covers only one photopeak. This would ensure that two detected photons indeed originate from the same cascade, with each having the appropriate energy, thereby suppressing random coincidences. However, because this approach would significantly reduce the statistics and since we correct for random coincidences anyway, we decided to adjust the energy windows so that both

SCAs cover both peaks.



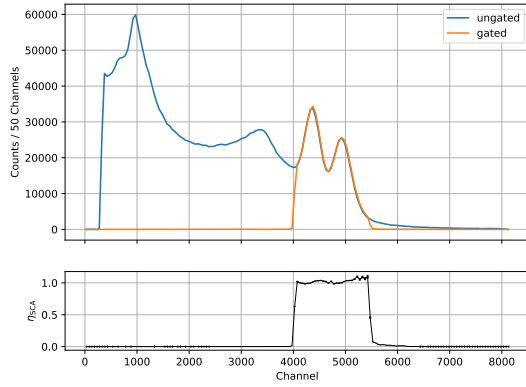
(a) Movable detector (D1)



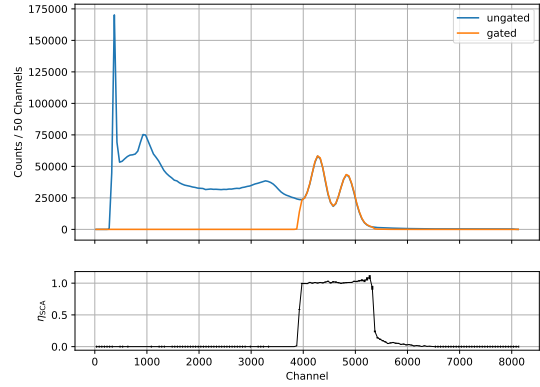
(b) Fixed detector (D2)

Figure 4.4.: Oscillogram corresponding to the circuit in Figure 4.3 used to calibrate the SCAs. The first channel (yellow) corresponds to the detector pulses, the second channel (pink) corresponds to the output signal of the SCA. Each square of the grid corresponds to 500 ns in the horizontal direction and 5 V in the vertical direction.

After setting the upper and lower thresholds for each SCA window, we measured the spectrum for 300 s twice: once without the gate signal (corresponding to the entire spectrum) and once with the gate signal (corresponding to the photopeaks within the selected window). This is shown in Figure 4.5.



(a) SCA1



(b) SCA2

Figure 4.5.: Adjustment of the SCA energy windows: Recorded spectra and calculated sensitivities for both SCAs.

Using these measurements, we can compute the so-called sensitivity of the SCAs,

which is given by the ratio of the recorded spectra:

$$\eta_{\text{SCA}}(E) = \frac{N_{\text{SCA-gated}}(E)}{N_{\text{self-gated}}(E)}.$$

Ideally, the sensitivity should be close to one within the range of the photopeaks and zero elsewhere.

Our MCA has 8192 channels. The number of counts in each channel has a Poisson error of  $\sqrt{N}$ . Because the spectrum was recorded only for a relatively short period, dividing the two raw spectra would yield relatively large fluctuations in the calculated sensitivity. For this reason, we first rebinned the spectra by combining 50 channels each. The sensitivity obtained by taking the ratio of the rebinned spectra is indeed nearly one inside the SCA windows and zero outside, as expected (see Figure 4.5).

### 4.3. Threshold Adjustment of the CFDs

The calibration of the CFDs in the fast branch is mostly analogous to the calibration of the SCAs in the slow branch. The main difference in the circuit (see Figure 4.6) is that the SCA is replaced by the CFD.

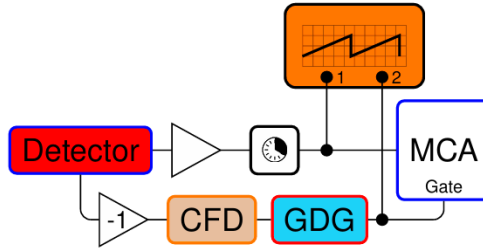


Figure 4.6.: Circuit used to adjust the CFD threshold. This is done for both detectors and the respective CFDs. Taken from [2].

First, we adjust the delay so that the detector pulses and the signals from the CFD overlap. This is done for both detectors, as shown in Figure 4.7. The next goal is to set the threshold of the CFD sufficiently high so that it is not triggered by electronic noise, while ensuring it is not so high that true signals are suppressed. To verify that our settings meet these conditions, we observe the CFD-gated MCA spectrum. We aim for this spectrum to encompass the photo peaks while excluding the lower-energy parts of the spectrum. However, since this part of the circuit is not intended for energy selection, unlike the SCA settings, we allow for a little more room next to the photo peaks.

After setting appropriate thresholds, we recorded the spectrum for both detectors over a period of 300 s with and without using the CFD signal as the gate for the MCA. The results are displayed in Figure 4.8.

The CFD sensitivity can be calculated analogously to that for the SCAs:

$$\eta_{\text{CFD}}(E) = \frac{N_{\text{CFD-gated}}(E)}{N_{\text{self-gated}}(E)}.$$



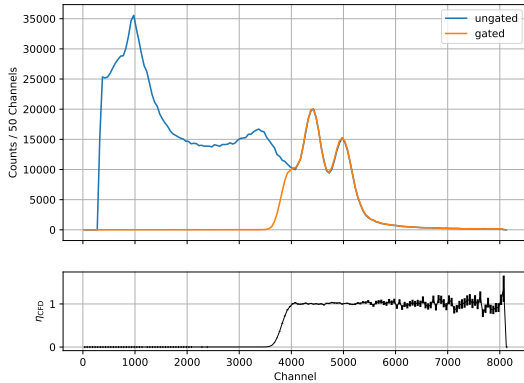
(a) Movable detector (D1)



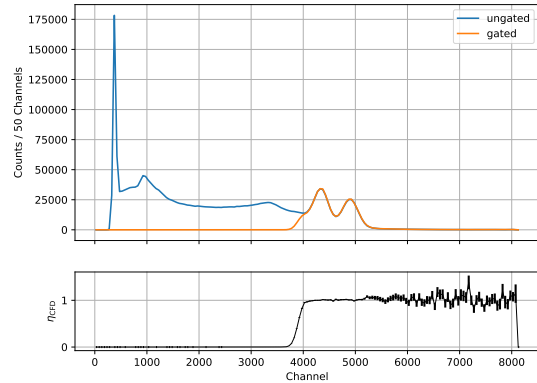
(b) Fixed detector (D2)

Figure 4.7.: Oscillogram corresponding to the circuit in Figure 4.6 used to set the CFD thresholds. The first channel (yellow) corresponds to the detector pulses, the second channel (pink) corresponds to the output signal of the CFD. Each square of the grid corresponds to 500 ns in the horizontal direction and 5 V in the vertical direction.

Again, we first rebinned the spectra by combining 50 channels before we calculated the sensitivity. As intended, the sensitivity is approximately one in the range of the photopeaks and vanishes for lower energies (see Figure 4.8).



(a) CFD1



(b) CFD2

Figure 4.8.: Adjustment of the CFD thresholds: Recorded spectra and calculated sensitivities for both CFDs.

#### 4.4. Delay Adjustment

After calibrating both the slow and fast branches of the circuit, we must still ensure that all signals arrive at the coincidence units simultaneously, as differences in cable lengths

and other effects can introduce delays. In this step, we adjust the delays to compensate for these differences so that all signals are time-aligned.

#### 4.4.1. Fast Branch

We first focus on the fast branch. The signals of both detectors need to be properly aligned in time before entering the fast coincidence. To achieve this, we set up the circuit shown in Figure 4.9.

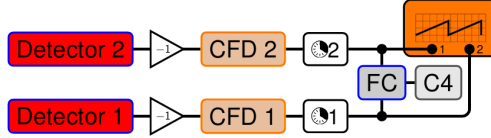


Figure 4.9.: Circuit used to adjust the delays in the fast branch. Taken from [2].

Each detector signal is amplified, sent to the CFD, and then passed through a ns delay. Next, both signals are fed into the FC and subsequently to counter C4. The counts on C4 depend on the relative delay. Therefore, by analyzing how the counts on C4 vary as a function of the relative delay (prompt curve), we can determine the ideal setting. We expect a constant background from random coincidences at all relative delays. If the time misalignment is not corrected by the relative delay, no additional counts are expected. However, over a certain range of relative delays, the alignment is sufficiently good to trigger the FC when a true coincidence occurs. In this range, we expect constant rates, resulting in a plateau. This behavior is described by the following function [1]:

$$f(t) = \frac{A}{2} \cdot \left( 1 + \operatorname{erf} \left( \frac{t - (t_0 - \frac{w}{2})}{\sigma} \right) \cdot \operatorname{erf} \left( \frac{(t_0 + \frac{w}{2}) - t}{\sigma} \right) \right) + A_0, \quad (4.1)$$

which we will fit to our measurement series. The parameters have the following meaning:

- $A_0$ : Offset caused by random coincidences. Since this should not depend on the relative delay, a constant is sufficient to describe it.
- $A$ : Number of coincidences at the plateau, excluding background events.
- $t_0$ : Center of the plateau.
- $\sigma$ : The width of the slope. This corresponds to the range of relative delays over which some, but not all, CFD pulses overlap.
- $w$ : The full width at half maximum of the curve, which corresponds to the resolving time.

The resolving time indicates the maximum time difference between two pulses that are still detected as coincident. The signals of a true coincidence will exhibit some

fluctuation in their arrival times. Thus, if the resolving time is too short, some true coincidences will not be detected. Conversely, if it is too long, signals with a larger time difference than that typical of true coincidences will also be counted as coincidences. In other words, the number and the fraction of random coincidences will increase.

The main aim of taking a measurement series for the prompt curve is to determine the parameter  $t_0$ . This parameter indicates where the signal overlap is maximal and thus provides the optimal setting for the delay. To determine the best choice for  $t_0$ , we adjust the ns delay to set various relative delays and for each measure the number of counts over a period of 20 s. The data are presented in Table A.1, where we assumed Poisson errors  $\sqrt{N}$  for the counts  $N$  recorded by C4.

We then fit the prompt curve (Eq. 4.1) to the data, yielding the parameters listed in Table 4.1. The reduced  $\chi^2$  value, which is close to one, indicates that the function chosen for the prompt curve is well suited to describe the data.

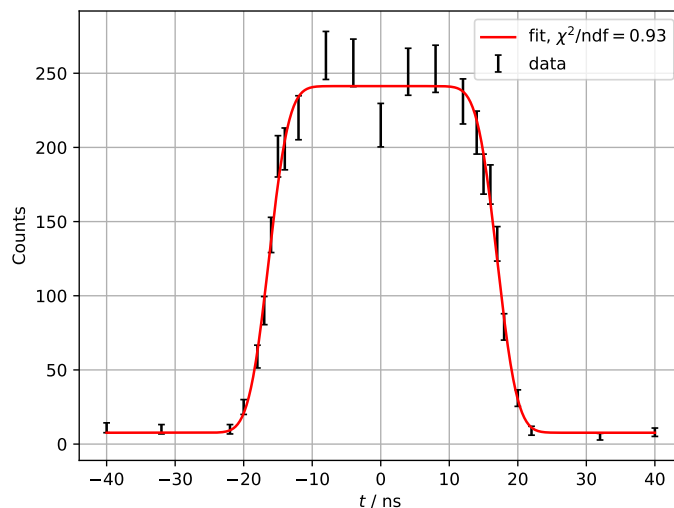


Figure 4.10.: FC counts as a function of the relative delay between the two CFD output signals. The data was fitted according to function 4.1.

Table 4.1.: Fit parameters obtained for the prompt curve (Figure 4.10).

$A / \text{s}^{-1}$	$A_0 / \text{s}^{-1}$	$t_0 / \text{ns}$	$w / \text{ns}$	$\sigma / \text{ns}$
234(6)	7.7(12)	0.33(9)	33.31(27)	-3.27(22)

According to Table 4.1, we find the optimal value for the relative delay in the fast branch to be 0.33(9) ns. However, since we can only adjust the relative delay in steps of 0.5 ns, we choose 0.5 ns as the final setting. The difference between these values is significantly smaller than the width  $w$  of the plateau ( $w = 33.31(27)$  ns), so we do not expect it to have a significant impact.



#### 4.4.2. Slow Branch

The final step is to align the SCA signals and the fast coincidence signal in time. This alignment is done by setting up the circuit shown in Figure 4.11. The setup is identical to the full setup discussed in Section 3 with the addition of the oscilloscope.

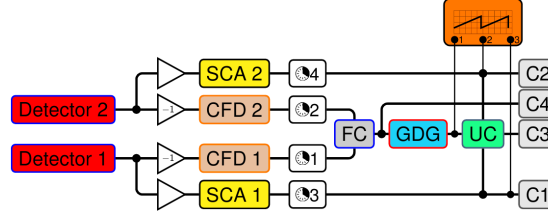


Figure 4.11.: Circuit used to adjust the delay in the slow branch. Taken from [2], edited by [1].

Using the oscilloscope, the pulses in both parts of the slow branch as well as in the fast branch are displayed. The goal is first to adjust the delays in the slow branch so that the signals overlap with those in the fast branch. Afterwards, the GDG is used to adjust the width of the fast branch pulse to match the width of the slow branch pulses. A smaller width could lead to true coincidences not always being detected, while a larger width would increase the number of random coincidences. We want to achieve maximal overlap, meaning that the centers should be aligned. However, we have also adjusted all lengths to be the same, which corresponds to aligning all edges as well. The result is shown in Figure 4.12.

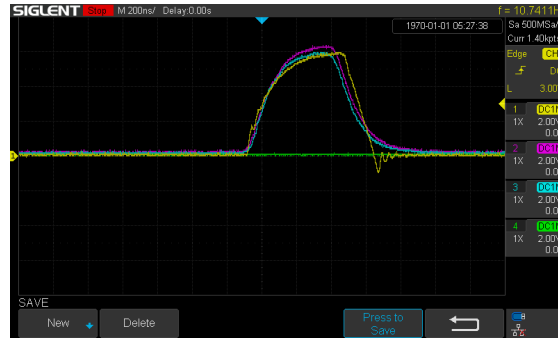


Figure 4.12.: Oscillogram corresponding to the circuit in Figure 4.11 used to adjust the delay in the slow branch. The first channel (yellow) corresponds to the signal of the fast branch after the GDG, the second channel (pink) corresponds to the detector 1 part of the slow branch and the third channel (blue) corresponds to the detector 2 part of the slow branch. Each square of the grid corresponds to 200 ns in the horizontal direction and 5 V in the vertical direction.

## 5. Main Measurement

After ensuring proper calibration and time alignment of the circuit's electronic components, we can now use our setup to measure the angular correlation of the cascaded  $^{60}\text{Ni}$  decay. Before doing so, it is necessary to discuss the optimal measurement distance, the angles at which to measure, and the role of random coincidences. The actual measurement is then performed automatized overnight. Its analysis involves studying the setup's stability, a correction of misalignments and the final angular correlation determination.

### 5.1. Choice of Detector Distances

In the experiment, we can choose the distance between the detectors and the source. First, we want to determine which distance leads to the smallest uncertainties. The closer the detectors are to the source, the larger the solid angle they cover. We can correct for this using the method introduced in [3], which provides a correction for the coefficients  $A_{kk}$  ( $k \in \{2, 4\}$ ) from Eq. 2.1:

$$A_{kk} = \frac{A_{kk}^{\text{exp}}}{Q_{kk}} = \frac{A_{kk}^{\text{exp}}}{Q_k(r_1)Q_k(r_2)}.$$

The goal of the experiment is to determine the coefficients  $A_{kk}$  with high accuracy, so we aim for a small uncertainty  $\Delta A_{kk}$ . We now make the reasonable assumption that  $\Delta A_{kk}^{\text{exp}}$  is roughly proportional to the relative uncertainty  $\Delta C/C$  of the measured coincidence rate  $C$ . The latter is proportional to the detector count rates  $\dot{N}_1$  and  $\dot{N}_2$ . Denoting the number of counts after a certain time as  $N_i$  and assuming Poisson errors  $\sqrt{N_i}$ , we obtain

$$\Delta A_{kk} = \frac{\Delta A_{kk}^{\text{exp}}}{Q_k(r_1)Q_k(r_2)} \propto \frac{\Delta C/C}{Q_k(r_1)Q_k(r_2)} \propto \frac{\sqrt{N_1}\sqrt{N_2}\sqrt{N_1+N_2}}{N_1N_2 Q_k(r_1)Q_k(r_2)}.$$

If the count rates are sufficiently large, the term  $\sqrt{N_1+N_2}$  approximately scales as  $\sqrt{N_1}$  or  $\sqrt{N_2}$ . To a good approximation, we therefore write

$$\Delta A_{kk} \propto \frac{1}{\sqrt{N_1}\sqrt{N_2} Q_k(r_1)Q_k(r_2)}.$$

Finally, using  $N_i \propto r_i^{-2}$  and assuming  $r_1 \approx r_2 \equiv r$ , we arrive at an expression that depends only on  $r$  and  $Q_k(r)$ :

$$\Delta A_{kk} \propto \frac{r^2}{Q_k(r)^2}. \quad (5.1)$$

In [3], several values for the correction factors  $Q_2$  and  $Q_4$  are provided. They are given for distances  $r$  of 10 cm, 7 cm, and 5 cm, as well as for different energies, including 1 MeV and 1.5 MeV at the photopeak. By inserting these values into Eq. 5.1, we can calculate the distance  $r$  at which we can expect the smallest uncertainties in  $A_{kk}$ . Since the photopeak in our case of the  $^{60}_{28}\text{Ni}^*$  decay lies between 1 MeV and 1.5 MeV, we take the average of the correction factors for these two energies. The results are listed in Table 5.1.

$r$ / cm	$Q_2$	$r^2/Q_2^2$ / cm <sup>2</sup>	$Q_4$	$r^2/Q_4^2$ / cm <sup>2</sup>
5	0.90515	30.514	0.71000	49.593
7	0.94405	54.980	0.82235	72.457
10	0.96890	106.52	0.8989	123.76

Table 5.1.: Ratio  $r^2/Q_k^2$ ,  $k \in \{2, 4\}$ , for different distances. We used the average of the  $Q_k$  values at 1 MeV and 1.5 MeV.

From the table, we deduce that  $r = 5$  cm is the best choice, as it should allow us to determine the coefficients  $A_{kk}$  with the highest accuracy. Therefore, this distance is used in the setup.

## 5.2. Choice of Measured Angles

In the experimental setup, one of the detectors is fixed, while the other is movable to vary the angle between the detectors. However, some angles may provide more insight than others. Therefore, we want to use the theoretical assumptions regarding the correlation function, as outlined in Section 2.2, to pre-select the most important angles. The angular correlation function can be expressed as

$$f(\theta) = A \left( 1 + B \cdot \cos^2(\theta) + C \cdot \cos^4(\theta) \right), \quad (5.2)$$

where  $A$  is a scaling factor which depends linearly on the measurement time, the distance between source and detectors, and the activity of the source. The coefficients  $B$  and  $C$  contain the correlation information and can be rewritten in terms of  $\alpha$  and  $\beta$

$$\alpha = B + C \quad \beta = B - C.$$

This approach is taken from [1]. By comparing Eq. 5.2 with Eq. 2.1 and inserting the explicit form of the Legendre polynomials as well as the predicted values for the coefficients  $A_{22}$  and  $A_{44}$ , we find  $B = \frac{1}{8}$  and  $C = \frac{1}{24}$ <sup>1</sup>. Consequently, the theoretically expected values for  $\alpha$  and  $\beta$  read:

$$\alpha_0 = \frac{1}{6} \quad \beta_0 = \frac{1}{12}.$$

---

<sup>1</sup>In fact, since [3] only states rounded decimal numbers for the theoretical prediction of  $A_{kk}$ , the results for  $B$  and  $C$  obtained in this way suffer from rounding errors as well. However, the precise values  $B = \frac{1}{8}$  and  $C = \frac{1}{24}$  can, for example, be looked up in [5]

To examine how changes in  $\alpha$  and  $\beta$  affect the correlation function, we have plotted the theoretical prediction alongside variations of these parameters in Figure 5.1. It is apparent that  $\alpha$  controls the height of the correlation function, while  $\beta$  determines its width. Due to the periodicity of the function, it is sufficient to measure within an interval from  $90^\circ$  to  $270^\circ$ . We conclude that to be sensitive to  $\alpha$ , we should measure the correlation function at its maximum at  $180^\circ$ . For determining  $\beta$ , it is useful to measure at the turning points at  $135^\circ$  and  $225^\circ$ . The remaining angles have approximately the same importance, so we distribute them equally throughout the interval. As a compromise between the number of angles and the total measurement time, we have decided to measure the following nine angles:

$$\theta \in \{90^\circ, 112.5^\circ, 135^\circ, 157.5^\circ, 180^\circ, 202.4^\circ, 225^\circ, 247.5^\circ, 270^\circ\} \quad (5.3)$$

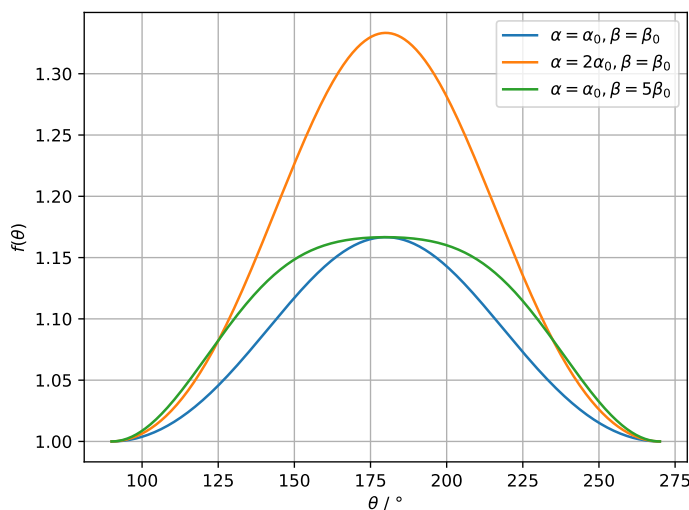


Figure 5.1.: Angular correlation function  $f(\theta)$  for the predicted values  $\alpha_0 = \frac{1}{6}$  and  $\beta_0 = \frac{1}{12}$ , as well as for two other parameter choices at  $A = 1$ .

### 5.3. Random coincidences

As mentioned in previous sections, not all coincident events correspond to the decay of a single nucleus. Noise and uncorrelated background events can also occur as coincidences. Two nuclei may decay within a time interval shorter than the resolving time, leading our setup to detect two emitted photons. However, using this circuit we cannot distinguish whether the photons were emitted from the same nucleus or from different ones. We expect these random coincidences to be independent of any delay within the circuit. Therefore, we can measure the random coincidence rate by setting the delay to a value that excludes the detection of true coincidences.

In practice, we chose a relative delay of 63 ns between the signals in the fast branch (instead of the 0.5 ns found in Section 4.4.1). This value is significantly larger than the resolving time determined in Section 4.4.1, so no true coincidences should be detected under these conditions. Before measuring the angular correlation, we will set this value back to 0.5 ns.

The longer the measurement period, the smaller the relative statistical uncertainties become (assuming Poisson errors  $\sqrt{N}$  again). However, due to time constraints, we had to make a compromise. We chose to perform the random coincidence measurement over a period of 300 s at each angle listed in 5.3. The results are shown in Figure 5.2.

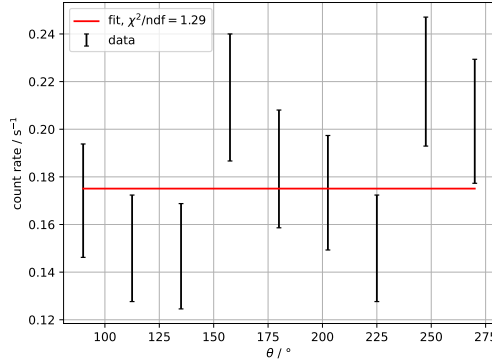


Figure 5.2.: Measurement of random coincidences. A constant function (red line) was fitted to obtain an average random coincidence of  $0.175(9) \text{ s}^{-1}$ .

The obtained rates are all of the same order of magnitude and do not significantly differ from each other. As expected, the random coincidence rates do not show any discernible dependence on the angle. Therefore, we performed a least-squares fit using a constant function to describe the data. This yielded an average random coincidence rate of  $0.175(9) \text{ s}^{-1}$ , which will later be subtracted from the main measurement.

## 5.4. Stability Analysis

The main measurement is conducted automatically overnight. In this process, the nine angles from 5.3 between the detectors are set in a computer-controlled manner and the respective count rates are recorded. Instead of performing one long measurement per angle, it makes sense to conduct several shorter measurements for each angular setting. This is because the electronic devices do not remain perfectly stable over the measurement period as, for example, the set gains and thresholds may change with temperature. If only one long measurement per angle were taken, it would result in relatively large systematic errors.

In our case, we set the individual measuring time to 600 s. In total, 11 measurement series per angle are recorded, with one run taken in ascending order from the smallest

to the largest angle and the following run taken in descending order from the largest to the smallest angle.

With these repeated measurements, we have the opportunity to specifically investigate the stability of the setup. For this purpose, we can examine the count rates of the counters as a function of the 11 time points at which the measurements were recorded. Ideally, with perfectly stable electronics, the count rates should remain constant within the statistical uncertainties.

The results of the stability analysis are shown in Figures 5.3 to 5.6. For each angle, the count rate of the respective counter is plotted against the measurement time. Since the angles were alternately measured in ascending and descending order, the data points are spaced at varying intervals.

A comparison of the figures immediately reveals the different orders of magnitude of the count rates. While Counters C1 and C2 (Figures 5.3 and 5.4) display the detection rates within the energy windows set by the SCAs, Counters C3 and C4 (Figures 5.5 and 5.6) measure the number of universal and fast coincidences, respectively, leading to significantly lower rates. As expected, the count rate of Counter C3 (universal coincidences) is slightly lower than that of C4 (fast coincidences), since C3 requires not only simultaneous photon detection but also fulfillment of the energy condition.

Next, we briefly consider the angular dependence of the count rates. Naturally, for the coincidence rates, we expect a behaviour similar to the one shown in Figure 5.1, which is the main focus of this experiment. However, for the single-detector count rates, we would naively expect no angular dependence. Nevertheless, as we will see in Section 5.5, a slight misalignment of the source from the exact center leads to an angular dependence in the count rate of the movable detector, which can already be observed in Figure 5.3. For the fixed detector, this effect does not occur, so the count rates in Figure 5.4 remain within the same order of magnitude.

To address the primary question of this section, whether and how the count rates changed over the course of the measurement, we fit the data points using the least-square method with linear functions of the form

$$r(t) = r_0 + s \cdot t, \quad (5.4)$$

where  $r(t)$  represents the measured count rate,  $t$  is the time in minutes,  $r_0$  is the initial count rate at  $t = 0$ , and  $s$  is the slope with which the count rate changes. The fit parameters for all fits can be found in Table A.2 in the Appendix. In all cases, the reduced  $\chi^2$  values are close to 1, indicating a good fit quality.

For a perfectly stable setup, all determined slopes  $s$  should be consistent with zero. While this is mostly true for the count rates of the movable detector (see Fig. 5.3 and Table A.3a), it is not the case for the fixed detector. As can be seen in Fig. 5.4 and Table A.3b, all slopes are negative, meaning that the count rates decreased over the measurement period.

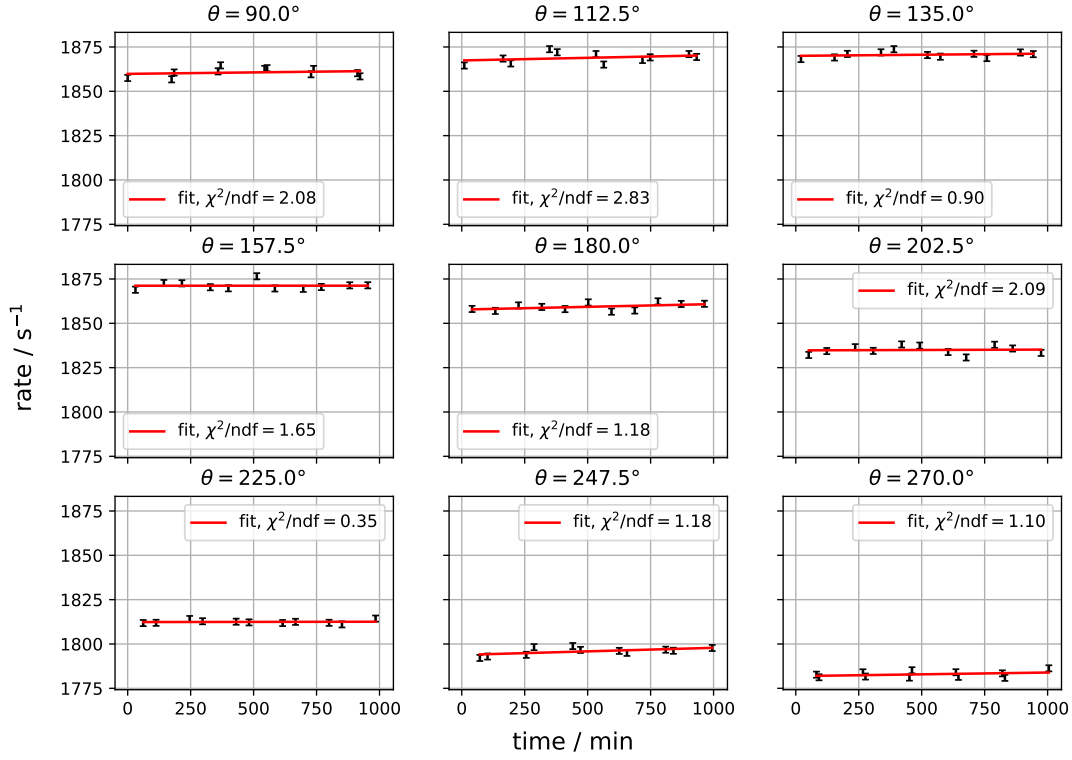


Figure 5.3.: Investigation of the stability of the movable detector's count rate (counter C1). For discussion, see the main text. The obtained fit parameters are listed in Table A.3a

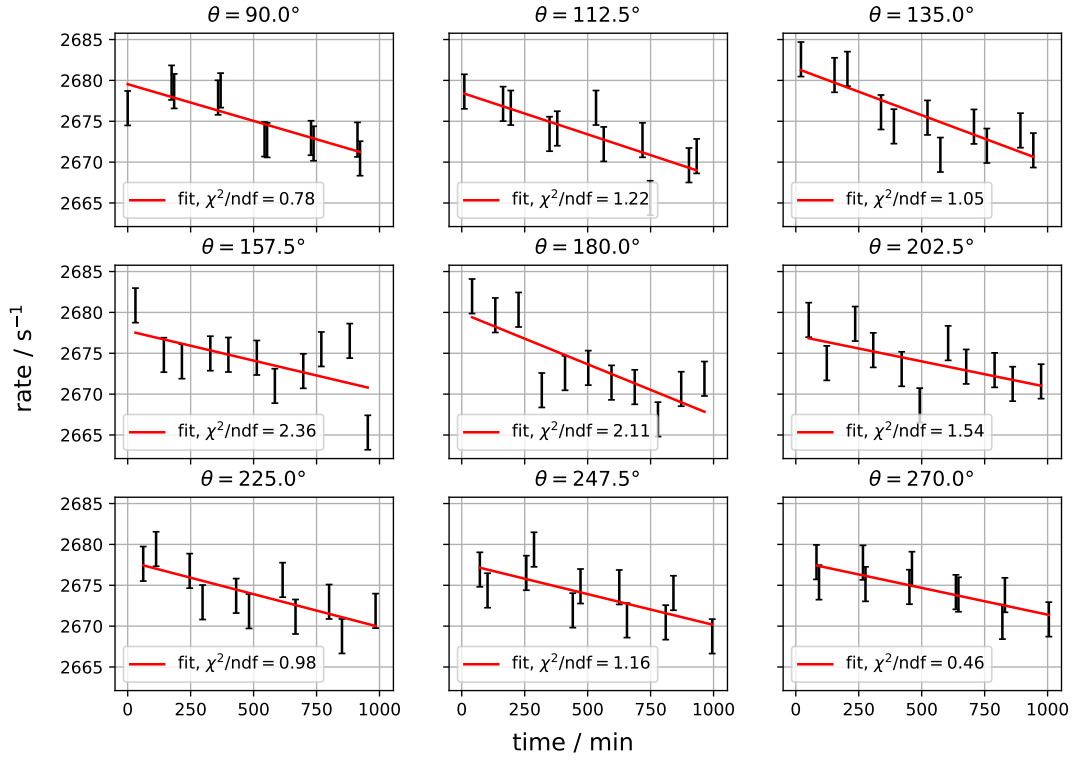


Figure 5.4.: Investigation of the stability of the fixed detector's count rate (counter C2). For discussion, see the main text. The obtained fit parameters are listed in Table A.3b

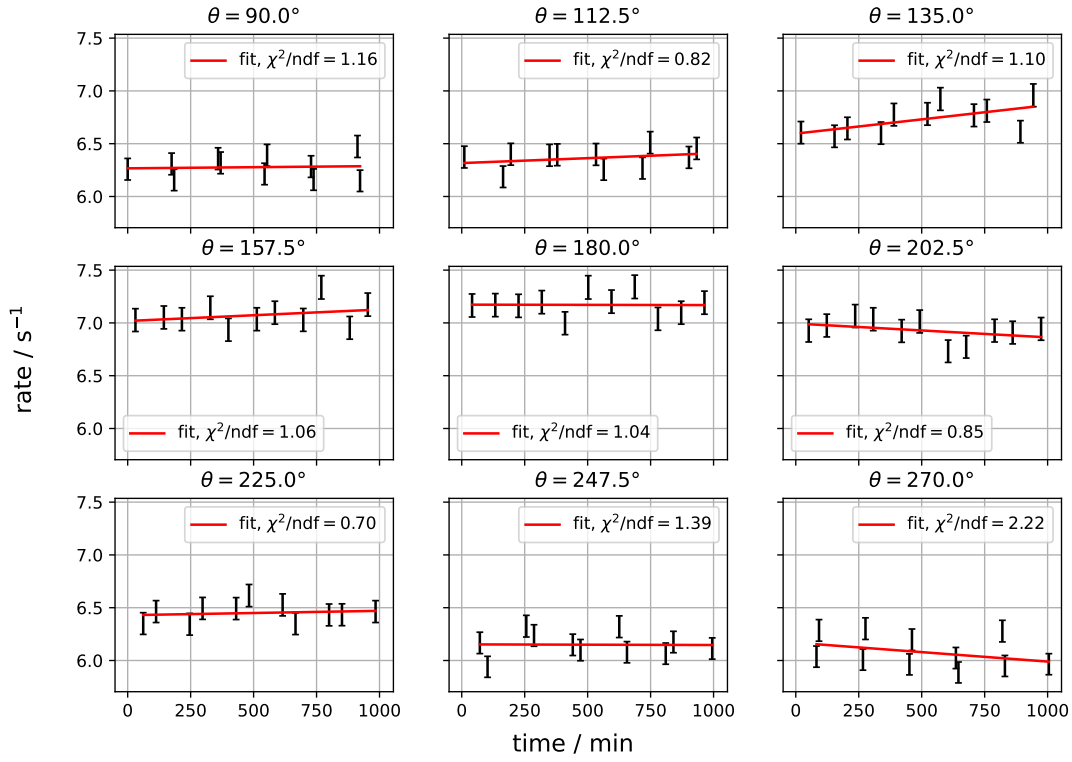


Figure 5.5.: Investigation of the stability of the universal coincidence count rate (counter C3). For discussion, see the main text. The obtained fit parameters are listed in Table A.3c

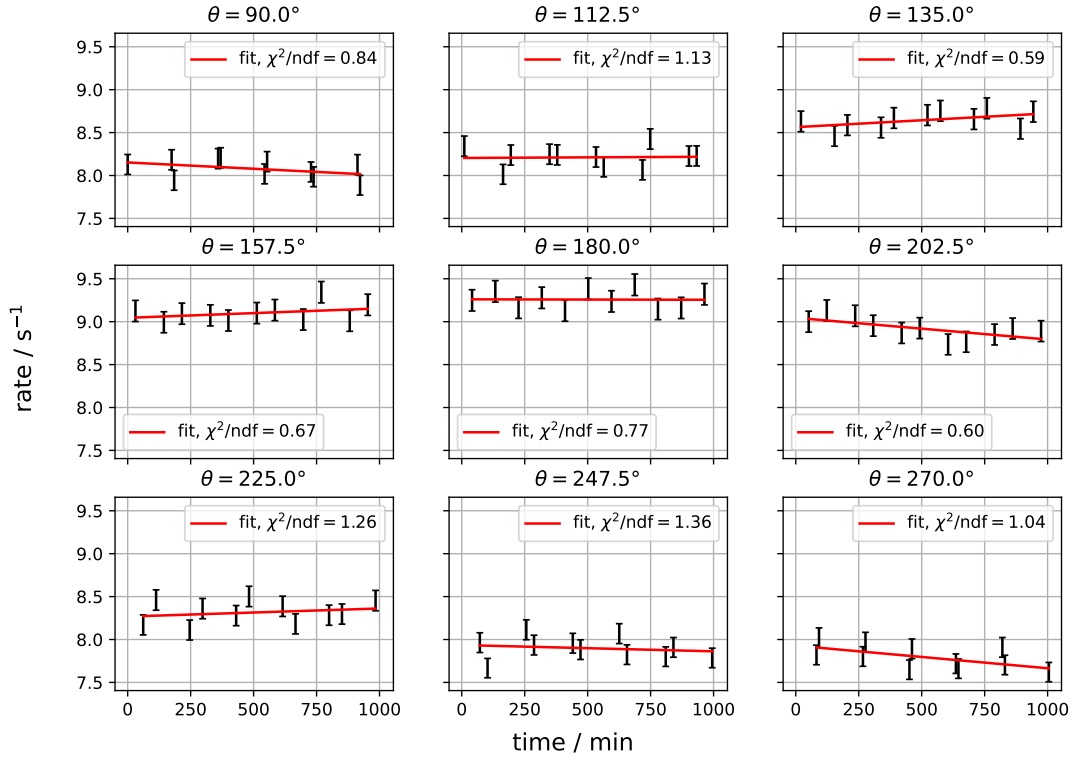


Figure 5.6.: Investigation of the stability of the fast coincidence count rate (counter C4). For discussion, see the main text. The obtained fit parameters are listed in Table A.3d



This indicates an actual instability in the setup. The most likely cause is a drop in temperature overnight, which affected the set gains and thresholds of the electronic components.

Since the coincidence rate is proportional to the individual detectors' count rates, one would naively expect a decline in coincidences over time as well. However, this cannot be inferred from the diagrams in Fig. 5.5 and Fig. 5.6. The determined slopes  $s$  (see Tables A.3c and A.3d) are mostly compatible with zero, showing no clear trend in a time-dependent change of the count rates. The decrease in the count rates of the fixed detector is apparently small enough that it does not noticeably affect the coincidence rate. Therefore, we refrain from correcting this systematic error, as it should not impact the determination of the angular correlation function.

## 5.5. De-adjustment Correction

In our experimental setup, the source is not necessarily positioned precisely at the center of the circle defined by the detectors. This misalignment may introduce systematic errors in the count rates at different positions. To account for these errors, we make the following considerations:

We assume that the detectors are arranged along a perfect circle with radius  $r$  and center  $C$ . As detector D1 moves along the circle, it forms an angle  $\theta$  with the fixed detector D2. Furthermore, we assume that the source, located at point  $S$ , has a small displacement  $\epsilon \ll r$  relative to the center  $C$ . We define  $\phi$  as the angle between  $\overline{SC}$  and  $\overline{CD1}$  and denote the distances between the source and the detectors as  $r_1$  and  $r_2$ , respectively (see Figure 5.8).

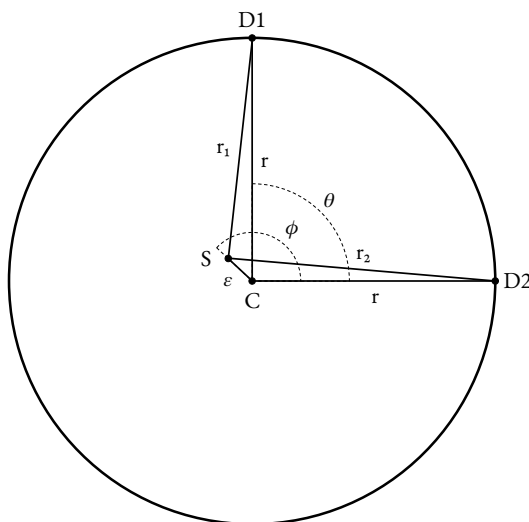


Figure 5.7.: Theoretical considerations for the de-adjustment correction.

Applying the law of cosines, we obtain:

$$r_1^2 = r^2 + \epsilon^2 - 2\epsilon r \cos(\phi - \theta) \quad \text{and} \quad r_2^2 = r^2 + \epsilon^2 - 2\epsilon r \cos(\phi),$$

where we can neglect the  $\epsilon^2$  terms. Consequently, as detector D1 moves along the circle, its distance  $r_1$  to the source varies. The count rate is proportional to the inverse square of the distance, meaning that we expect for  $\dot{N}_1(\theta)$ :

$$\dot{N}_1(\theta) \propto \frac{1}{r_1^2} = \frac{1}{r^2 - 2\epsilon r \cos(\phi - \theta)} \quad (5.5)$$

To check whether our theoretical considerations are sensible, we performed a fit according to Eq. 5.5, where we set  $r = 5$  cm as discussed earlier. In this case, we summed the counts and times from all single measurements to calculate an average count rate. The result is depicted in Figure 5.8.

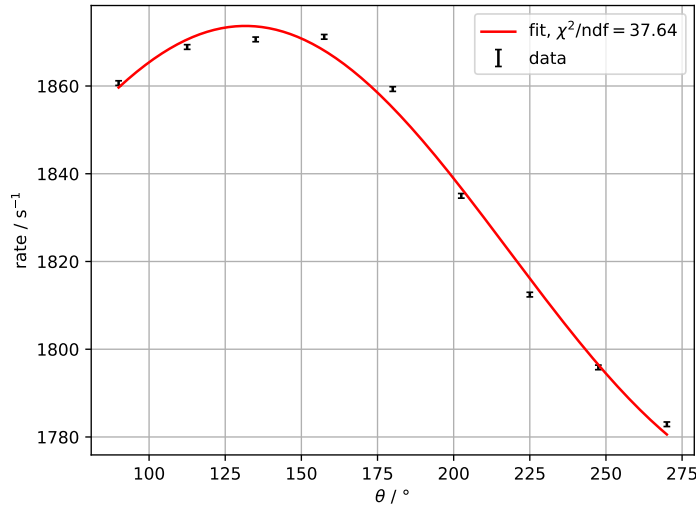


Figure 5.8.: Count rates of the movable detector as a function of the angle. A function of the type given in Eq. 5.5 was fitted to the data (red line).

The determined fit parameters are  $\epsilon = 0.726(30)$  mm and  $\phi = 131.6(25)^\circ$ . The fit quality, with a reduced  $\chi^2$  of 37.64, is worse than in the previous fits. This is due to the fact that the error bars are relatively small because of averaging the rates, and our model is still not perfect, as it, for example, does not account for the spatial extent of the source. Nevertheless, the fit captures the overall trend of the data well.

Since the coincidence rate is proportional to  $\dot{N}_1$ , it exhibits the same angular dependence and must therefore be corrected. To do this, we define a correction factor  $K(\theta)$ , normalized such that  $K(\phi) = 1$ :

$$K(\theta) = \frac{r^2 - 2\epsilon r \cos(\phi - \theta)}{r^2 - 2\epsilon r} \quad (5.6)$$

We calculate the uncertainty of this factor by Gaussian error propagation and then multiply the coincidence rates by it.

## 5.6. Angular Correlation

After all influences of the setup on the measurement have been sufficiently understood, the angular correlation of the cascaded decay can finally be determined. For this purpose, we calculate the average rate of the universal coincidences (counter C3) from all individual measurements, correct the values using the factors from Eq. 5.6, and subtract the rate of random coincidences (see Section 5.3). The resulting rates are plotted against the angle, as shown in Figure 5.9. A least-squares fit of the theoretically predicted correlation function (Eq. 2.1) is then applied.

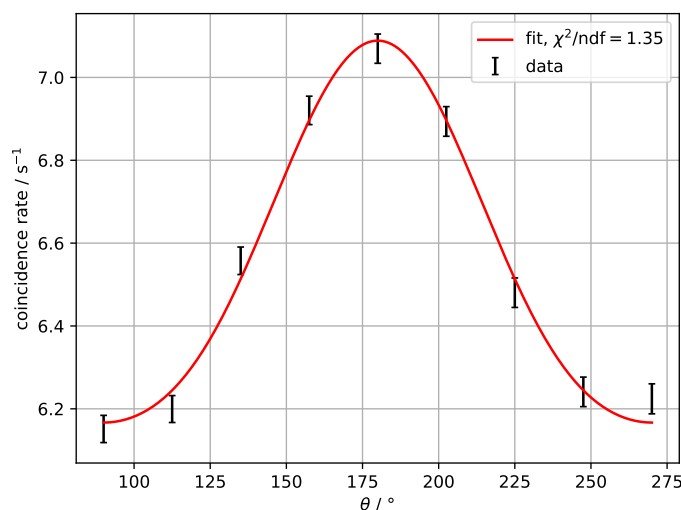


Figure 5.9.: Coincidence rate as a function of the angle. The averaged rates were corrected for misalignment and random coincidences and the theoretically predicted correlation function was fitted to the data (red line).

The fit function captures the data points well, as reflected by the reduced  $\chi^2$  value being close to 1. The obtained fit parameters are  $A_{22}^{\text{exp}} = 0.089(4)$  and  $A_{44}^{\text{exp}} = 0.016(5)$ . As we saw in Section 5.1, the coefficients  $A_{kk}^{\text{exp}}$  must be corrected because the detectors cover a non-negligible solid angle. As correction factors, we use, as previously in Table 5.1, the average of the factors for the energies 1.0 MeV and 1.5 MeV:

$$Q_2 = 0.90515 \quad Q_4 = 0.7100.$$

After dividing by these factors,

$$A_{kk} = \frac{A_{kk}^{\text{exp}}}{Q_{kk}} = \frac{A_{kk}^{\text{exp}}}{Q_k(r)Q_k(r)},$$

the following results are obtained from our fit parameters:

$$A_{22} = 0.109(5) \quad A_{44} = 0.032(10).$$

These values do not exactly match the theoretically predicted coefficients  $A_{22} = 0.1020$  and  $A_{44} = 0.0091$ , but they are consistent with them within a  $2\sigma$  and  $3\sigma$  interval, respectively. Notably, the relative uncertainty of the coefficient  $A_{44}$  is significantly larger than that of  $A_{22}$ . This is probably due to the fact that the  $\cos^4(\theta)$  component of the functional form (whose strength is given by  $A_{44}$ ) is difficult to determine accurately with the relatively few data points used in the fit. A measurement with more data points could likely yield more accurate results.

Finally, we want to investigate to what extent the theoretical curves for other possible cascades agree with our data. For this purpose, we use the form of the correlation function given in Eq. 5.2. For the coefficients  $B$  and  $C$ , we insert the theoretically predicted values for various other cascades from [5] and allow the overall amplitude  $A$  to vary in the fit. The result is shown in Figure 5.10. Even at first glance, it is apparent that no other correlation function adequately describes the data. The reduced  $\chi^2$  values also confirm that the only explanation for the observed distribution of coincidence rates is a  $4(2)2(2)0$  cascade.

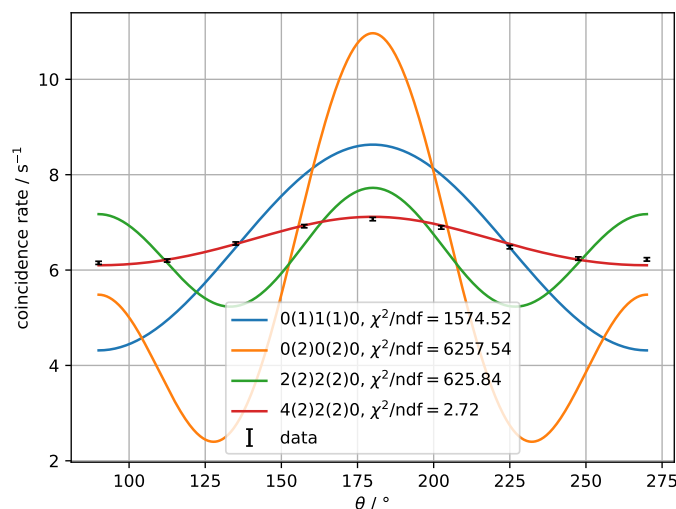


Figure 5.10.: Attempt to fit the measured coincidence distribution with theoretically predicted correlation functions of alternative cascades. Obviously, no other cascade except for the  $4(2)2(2)0$  cascade reasonably describes the data.

## 6. Conclusion

In this experiment, we investigated the angular correlation of a cascaded  $^{60}_{28}\text{Ni}^*$  decay. For this measurement, we set up a fast-slow coincidence circuit step by step. We ensured proper energy selection in the slow branch by calibrating the SCAs and proper time selection by adjusting the relative delay in the fast branch. Using an MCA, we calculated the sensitivities of both the SCAs and CFDs. As expected, both were close to 1 in the range of the photopeaks and zero elsewhere.

With proper time alignment of all signals, the calibration phase was successfully completed. For the subsequent measurements, we decided to use nine equally distributed angles. After measuring the random coincidences at each angle, the angular correlation was measured overnight. During this process, the count rates for each angle were recorded several times to reduce systematic errors and to study the setup's stability. In doing so, we found that the count rate of the fixed detector decreased over time, instead of remaining constant as would be expected for an ideal setup. However, this change in the count rate was apparently small enough that it did not affect the measured coincidence rate.

After correcting the coincidence rates for random coincidences and the setup's misalignment, a fit was performed to determine the angular correlation coefficients. Taking into account the solid angle corrections, these coefficients were determined to be

$$A_{22} = 0.109(5) \quad \text{and} \quad A_{44} = 0.032(10),$$

which are consistent with the theoretical predication within a  $2\sigma$  and  $3\sigma$  interval, respectively. By fitting the theoretical angular correlation functions for different cascades to the data, we ruled out that any cascade other than the  $4(2)2(2)0$  cascade caused the observed distribution of coincidence rates.

# A. Appendix

## A.1. Prompt Curve

Table A.1.: Measurement of the counts C4 as a function of the relative delay in the fast branch.

relative delay / ns	counts $N$
-40	11(3)
-32	10(3)
-22	10(3)
-20	25(5)
-18	59(8)
-17	90(9)
-16	141(12)
-15	194(14)
-14	199(14)
-12	220(15)
-8	262(16)
-4	257(16)
0	215(15)
4	251(16)
8	253(16)
12	231(15)
14	210(14)
15	182(13)
16	175(13)
17	135(12)
18	79(9)
20	31(6)
22	9(3)
32	5(2)
40	8(3)

## A.2. Stability Analysis

Table A.2.: Fit parameters for the stability analysis.

$\theta / ^\circ$	$r_0 / \text{s}^{-1}$	$s / \text{s}^{-1} \text{ min}^{-1}$
90.0	1860(2)	0.0016(26)
112.5	1867(2)	0.0030(31)
135.0	1870(1)	0.0013(17)
157.5	1871(1)	0.0000(23)
180.0	1858(1)	0.0031(20)
202.5	1835(2)	0.0004(26)
225.0	1812(1)	0.0002(11)
247.5	1794(1)	0.0040(19)
270.0	1782(1)	0.0020(19)

(a) Movable detector (counter C1)

$\theta / ^\circ$	$r_0 / \text{s}^{-1}$	$s / \text{s}^{-1} \text{ min}^{-1}$
90.0	2680(1)	-0.0090(19)
112.5	2678(1)	-0.0102(24)
135.0	2681(1)	-0.0115(22)
157.5	2678(2)	-0.0073(33)
180.0	2680(2)	-0.0125(32)
202.5	2677(2)	-0.0063(27)
225.0	2678(1)	-0.0080(21)
247.5	2678(1)	-0.0075(23)
270.0	2678(1)	-0.0066(15)

(b) Fixed detector (counter C2)

$\theta / ^\circ$	$r_0 / \text{s}^{-1}$	$s / \text{s}^{-1} \text{ min}^{-1}$
90.0	6.3(1)	0.000 02(11)
112.5	6.3(1)	0.000 09(10)
135.0	6.6(1)	0.000 27(11)
157.5	7.0(1)	0.000 11(12)
180.0	7.2(1)	0.000 00(12)
202.5	7.0(1)	-0.000 13(10)
225.0	6.4(1)	0.000 04(9)
247.5	6.2(1)	0.000 00(12)
270.0	6.2(1)	-0.000 18(15)

(c) Universal coincidences (counter C3)

$\theta / ^\circ$	$r_0 / \text{s}^{-1}$	$s / \text{s}^{-1} \text{ min}^{-1}$
90.0	8.2(1)	-0.000 15(11)
112.5	8.2(1)	0.000 02(13)
135.0	8.6(1)	0.000 16(9)
157.5	9.0(1)	0.000 11(10)
180.0	9.3(1)	-0.000 01(11)
202.5	9.0(1)	-0.000 25(10)
225.0	8.3(1)	0.000 09(14)
247.5	7.9(1)	-0.000 07(14)
270.0	7.9(1)	-0.000 26(12)

(d) Fast coincidences (counter C4)

# List of Figures

2.1. Decay scheme of $^{60}_{27}\text{Co}$ . . . . .	2
3.1. Detector setup . . . . .	4
3.2. Full setup of the fast-slow coincidence. . . . .	5
4.1. Circuit used to adjust the gain of the amplifier. . . . .	7
4.2. Oscillograms of the detector pulses after amplification . . . . .	8
4.3. Circuit used to set the windows of the SCAs. . . . .	8
4.4. Oscillogram used to calibrate the SCAs. . . . .	9
4.5. Adjustment of the SCA energy windows: Recorded spectra and calculated sensitivities for both SCAs. . . . .	9
4.6. Circuit used to adjust the CFD threshold. . . . .	10
4.7. Oscillogram used to set the CFD thresholds. . . . .	11
4.8. Adjustment of the CFD thresholds: Recorded spectra and calculated sensitivities for both CFDs. . . . .	11
4.9. Circuit used to adjust the delays in the fast branch. . . . .	12
4.10. FC counts as a function of the relative delay between the two CFD output signals. . . . .	13
4.11. Circuit used to adjust the delay in the slow branch. . . . .	14
4.12. Oscillogram used to adjust the delay in the slow branch. . . . .	14
5.1. Angular correlation function . . . . .	17
5.2. Measurement of random coincidences. . . . .	18
5.3. Investigation of the stability of the movable detector's count rate (counter C1). . . . .	20
5.4. Investigation of the stability of the fixed detector's count rate (counter C2) . . . . .	20
5.5. Investigation of the stability of the universal coincidence count rate (counter C3). . . . .	21
5.6. Investigation of the stability of the fast coincidence count rate (counter C4). . . . .	21
5.7. Theoretical considerations for the de-adjustment correction. . . . .	22
5.8. Count rates of the movable detector as a function of the angle. . . . .	23
5.9. Coincidence rate as a function of the angle. . . . .	24
5.10. Attempt to fit the measured coincidence distribution with theoretically predicted correlation functions of alternative cascades. . . . .	25



# List of Tables

4.1. Fit parameters obtained for the prompt curve (Figure 4.10). . . . .	13
5.1. Ratio $r^2/Q_k^2$ , $k \in \{2, 4\}$ , for different distances. . . . .	16
A.1. Measurement of the counts C4 as a function of the relative delay in the fast branch. . . . .	27
A.2. Fit parameters for the stability analysis. . . . .	28

# Bibliography

- [1] University of Bonn. *Nuclear  $\gamma\gamma$  Angular Correlations. Course Manual*. January 2024.
- [2] Peter Rosinsky. *Aufbau und Testung der Automatisierung winkelabhängiger  $\gamma$ -Messungen im Praktikum mit Hilfe einer motorisierten Messapparatur*. Bachelor's Thesis. University of Bonn. 2022.
- [3] Kai Siegbahn. *Alpha-, Beta- and Gamma-Ray Spectroscopy, Vol. 2*. North Holland Publishing Company, 1965.
- [4] William R. Leo. *Techniques for Nuclear and Particle Physics Experiments*. Springer, 1994. DOI: 10.1007/978-3-642-57920-2.
- [5] Robley D. Evans. *The Atomic Nucleus*. McGraw-Hill, Inc., 1955.